

ViDAR: Video Diffusion-Aware 4D Reconstruction From Monocular Inputs

Michal Nazarczuk^{1*} Sibi Catley-Chandar^{1,2*} Thomas Tanay¹
Zhensong Zhang¹ Gregory Slabaugh² Eduardo Pérez-Pellitero¹

¹ Huawei Noah's Ark Lab ² Queen Mary University of London

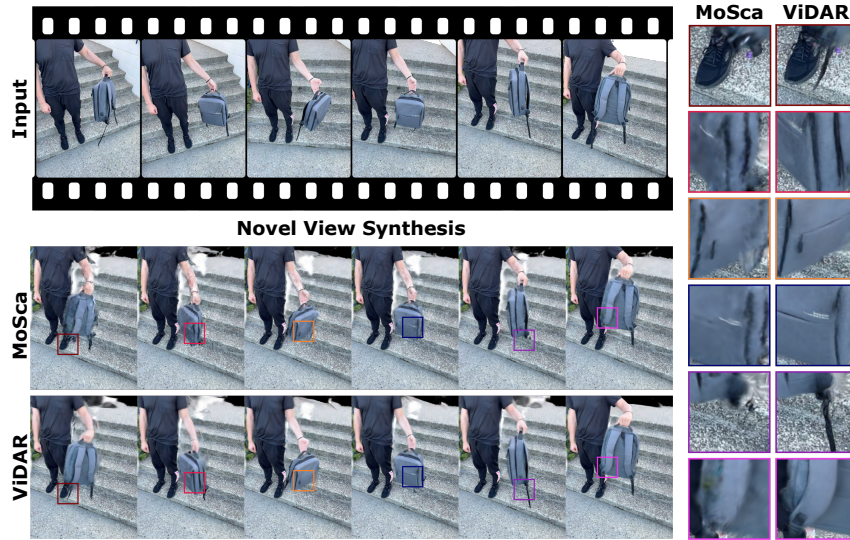


Figure 1: ViDAR provides a novel framework for Monocular Novel View Synthesis utilising a diffusion-aware reconstruction framework.

Abstract

Dynamic Novel View Synthesis aims to generate photorealistic views of moving subjects from arbitrary viewpoints. This task is particularly challenging when relying on monocular video, where disentangling structure from motion is ill-posed and supervision is scarce. We introduce Video Diffusion-Aware Reconstruction (ViDAR), a novel 4D reconstruction framework that leverages personalised diffusion models to synthesise a pseudo multi-view supervision signal for training a Gaussian splatting representation. By conditioning on scene-specific features, ViDAR recovers fine-grained appearance details while mitigating artefacts introduced by monocular ambiguity. To address the spatio-temporal inconsistency of diffusion-based supervision, we propose a diffusion-aware loss function and a camera pose optimisation strategy that aligns synthetic views with the underlying scene geometry. Experiments on DyCheck, a challenging benchmark with extreme viewpoint variation, show that ViDAR outperforms all state-of-the-art baselines in visual quality and geometric consistency. We further highlight ViDAR’s strong improvement over baselines on dynamic regions and provide a new benchmark to compare performance in reconstructing motion-rich parts of the scene. Project page: <https://vidar-4d.github.io/>.

*equal contribution

1 Introduction

4D reconstruction from monocular inputs is a challenging problem where the goal is to recover a 3D representation of a dynamic scene. It is increasingly important for modelling, comprehending, and interacting with the physical world and supports a wide range of downstream applications, ranging from augmented reality to generating data for training robust AI models [54].

Casually captured monocular videos are ubiquitous, however reconstructing 3D structure from them remains an inherently ill-posed problem. Static regions of the scene can typically be reconstructed well due to effective multi-view capture [4]. However for dynamic regions, depth information is not directly observable from a single viewpoint; in other words, it is difficult to disentangle the motion of the camera from motion within the scene. To mitigate this ambiguity many existing approaches impose strong regularisation [6; 28; 55] in the form of geometric assumptions, such as the object’s rigidity, that constrains the dynamics of the scene. Others [11; 23; 44; 62; 63] leverage learned priors, particularly those derived from large-scale models (*e.g.* monocular depth), to guide the reconstruction. While regularization based methods [11; 44] achieve geometrically compact scene representations, they often fall short in rendering high-quality, photorealistic appearances. Conversely recent generative approaches utilise powerful diffusion models to achieve higher visual quality in tasks such as single image to 3D [19; 21; 22; 50; 51; 64] and monocular reconstruction [48] but struggle to maintain spatio-temporal coherence, limiting their applicability in scenarios that demand accurate spatial reconstruction and temporal consistency, particularly in dynamic, real-world settings.

To tackle these challenges, we present Video Diffusion-Aware 4D Reconstruction (ViDAR), a monocular video reconstruction approach that leverages diffusion models as powerful appearance priors through a novel diffusion-aware reconstruction framework, which allows for improving visual fidelity without the loss of spatio-temporal consistency. We first train a monocular reconstruction baseline and generate a set of typically degraded multi-view images by sampling diverse camera poses and rendering the novel viewpoints. We then adopt a DreamBooth-style personalisation strategy [35], and tailor a pretrained diffusion model to the input video, which we use as a generative enhancer to inject rich visual information back into the degraded renders. This effectively generates a set of high-fidelity pseudo-multi-view observations for our scene, although due to the nature of the diffusion process, the resulting images are not necessarily spatially consistent. We observe that naively using these views as supervision leads to reconstructions degraded by artefacts and geometric inconsistencies. To mitigate this, we propose a method of diffusion-aware reconstruction, which selectively applies diffusion-based guidance to dynamic regions of the scene while jointly optimising the camera poses associated with the diffused views.

To the best of our knowledge, ViDAR is the first approach to incorporate a diffusion prior into monocular video reconstruction in a geometrically consistent manner. We demonstrate substantially improved qualitative and quantitative results compared to existing techniques (see Tabs. 1, 2, Figs. 1, 4), highlighting the effectiveness of diffusion-guided supervision when integrated with a reconstruction pipeline that accounts for geometric consistency.

We summarise our contributions as follows:

1. A personalised diffusion enhancement strategy that improves appearance quality by refining newly sampled renderings using a DreamBooth-adapted model.
2. A diffusion-aware reconstruction framework that combines dynamic-region-focused diffusion guidance with joint optimisation of the sampled camera poses for geometrically consistent reconstruction.
3. An extensive experimental evaluation, including both quantitative and qualitative comparisons with prior work, the introduction of a dynamic-region specific benchmark, as well as ablation studies isolating the impact of each component.

2 Related work

4D reconstruction Advances in novel view synthesis include the introduction of two seminal reconstruction paradigms, namely Neural Radiance Fields (NeRF) [27] and 3D Gaussian Splatting (3DGS) [9]. These developments in static scene reconstruction were quickly followed by several works on dynamic content. NeRF-based methods for video reconstruction include D-NeRF [33], StreamRF [13], HexPlane [2], K-Planes [3], Tensor4D [36], MixVoxels [43]. Similarly, Gaussian

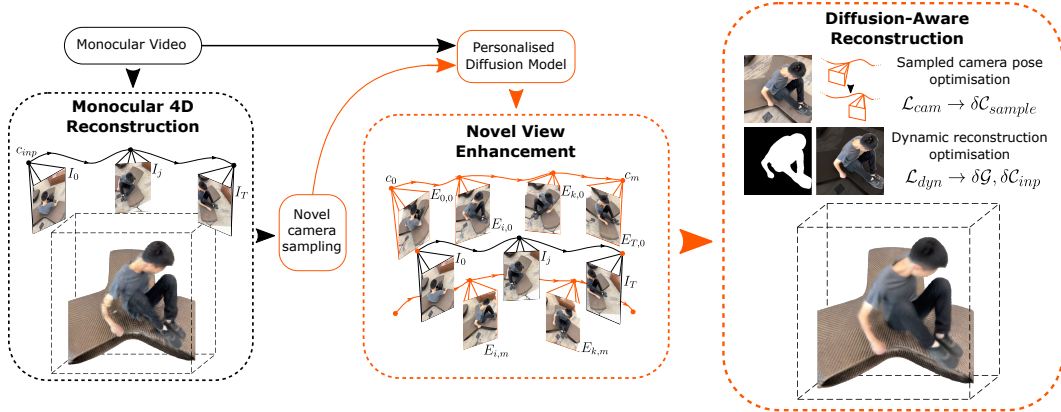


Figure 2: A high-level overview of ViDAR. The input video is used to create a 4D reconstruction with a monocular approach. Further, novel camera views are sampled and enhanced with a personalised diffusion model for each scene. This constitutes a set of pseudo-multi-view supervision examples. Finally, our approach optimises the 4D representation with the use of original video and new multi-view cues, in a diffusion-aware manner.

Splatting developments enabled research on dynamic novel view synthesis. Multi-view videos were reconstructed by: GaussianFlow [20], 4DGS [47], STG [16], SWinGS [37], Ex4DGS [10].

Monocular reconstruction The task of 4D monocular video reconstruction can be seen as a special case of 4D reconstruction under substantially more challenging conditions. This is due to the problem often being ill-posed: many of the target object surfaces may be seen only from one viewpoint throughout the video. Notably, among NeRF-based approaches, NSFF [14] proposes a time varying flow field, whereas Nerfies [29], HyperNeRF [30], DyCheck (T-NeRF) [4], DyBluRF [1], RoDynRF [24], CTNeRF [26] use a canonical representation with a time-dependent deformation. DynIBaR [15] uses Image Based Rendering for reconstruction. With Gaussian Splatting advancements, Dynamic 3D Gaussians [25] learn explicit motion of every Gaussian, whereas 4DGS [47], Deformable 3DGS [55], SC-GS [6] use a deformation field for transformation from canonical space. SplineGS [28] constrains the motion of Gaussians to splines to ensure temporal smoothness. DynPoint [62] and MotionGS [63] use an optical flow estimator for additional supervision. PGDVS [61] and BTimer [17] propose a transformer-based approach for generalisable reconstruction. Dynamic Gaussian Marbles [40] adopt a divide-and-conquer strategy to merge sets of Gaussians and create long trajectories, and restrict representation to isotropic Gaussians. MoDGS [23] improves the supervision from depth priors. D-NPC [7] proposes the use of neural implicit point cloud as the representation for monocular reconstruction. MoSca [11] and Shape of Motion [44] both utilise priors from pretrained foundational models (depth, optical flow, 2D tracking). Similarly, they both reconstruct static and dynamic content separately, and describe the motion of the Gaussians with lower dimensionality basis functions.

Diffusion enhanced reconstruction Several recent approaches explore the use of diffusion models to guide the reconstruction. ReconFusion [49] trains a diffusion model on a set of object images, and uses it to score the quality of sparse reconstruction, guiding it with RGB loss. DpDy [42] uses Score Distillation Sampling (SDS) [32] to supervise reconstruction with the use of image and depth diffusion model. CAT4D [48], concurrent to our work, uses a video-diffusion model to generate additional static cameras for the input video, followed by the reconstruction process. MVGD [5] proposes a direct rendering of novel views and depth as a conditional generative task. Other diffusion-based approaches include text or a single image to 3D generation [12; 18; 19; 21; 22; 38; 41; 46; 50; 51; 52; 56; 58; 59; 64]. Notably, our approach uses a monocular video as an input, and uses a personalised diffusion model along with our diffusion-aware reconstruction for accurate geometry modelling.

3 Method

Our method incorporates several stages which can be seen in Figure 2. Firstly, we use a monocular reconstruction baseline to obtain a 4D representation of the scene (Sec. 3.1), and generate a set of

degraded multi-view renders from sampled novel camera poses. Next, we personalise a diffusion model using the input video (Sec. 3.2), which is used to enhance the degraded renders (Sec. 3.2.1). Finally, we use the new set of enhanced pseudo-multi-view images to supervise and refine the 4D representation of the scene (Sec. 3.3), in a diffusion-aware manner.

3.1 Monocular Reconstruction

Given a casual monocular video of a dynamic scene with T frames $\mathcal{I} = [I_1, I_2, \dots, I_T]$, we perform initial reconstruction of the scene using an off-the-shelf 4D monocular reconstruction method, specifically, we use MoSca [11] in our implementation. The method reconstructs two sets of Gaussians for the given scene, namely static Gaussians \mathcal{G}_s , and dynamic Gaussians \mathcal{G}_d , that together create the scene representation: $\mathcal{G} = \mathcal{G}_d \cup \mathcal{G}_s$. MoSca leverages several priors in the reconstruction process: depth, optical flow, 2D tracking. Firstly, the optical flow is used to estimate the epipolar error and to determine the likelihood of image regions belonging to dynamic or static content. This is followed by the joint reconstruction of the static part of the scene \mathcal{G}_s and fine-tuning of the input camera pose c_{inp} . With that, a *scaffold*, a low dimensionality motion representation, is built through lifting 2D tracklets belonging to dynamic regions into 3D using depth information. Finally, a photometric reconstruction is performed to optimise the scene \mathcal{G} , enabling rendering of novel views R of the scene.

3.1.1 Track Anything Gaussian Classification

We note that the epipolar error analysis introduced by MoSca for classification of dynamic parts of the image leads to occurrences of floater artefacts due to the inclusion of background among dynamic Gaussians. This may not be reflected heavily in quantitative performance, but leads to a decrease in the quality of generated pseudo-multi-view samples (Sec. 3.2.1). To improve the constraint on dynamic Gaussians’ locations, we use dynamic masks D_t obtained from Track Anything [53] to reconstruct the static part of the scene \mathcal{G}_s and generate motion scaffolds (as in MoSca [11]).

3.2 Diffusion Enhancement

We utilise a Stable Diffusion [34] model, specifically the pretrained Stable Diffusion XL (SDXL) [31] to improve the quality of rendered images and guide the reconstruction process. Following the observations of ReconFusion [49], we decide to use a multistep denoising process, in contrast to Score Distillation Sampling [32]. Conversely, given a sampled image $R_{m,t}$ from camera c_m at the time t , we follow a standard text-to-image [34] process and encode the image into latent space: $x_0 = \mathcal{E}(R_{m,t})$. Further, instead of generating the noisy latent for image generation, we introduce k steps of noise into the image-sourced latent $x_0 \rightarrow x_k$ using the original noise scheduler (here, Discrete Euler [8]). We then follow the denoising process for k steps to achieve a denoised latent \hat{x}_0 which is then decoded to an enhanced version of the input image: $E_{m,t} = \mathcal{D}(\hat{x}_0)$.

Personalisation Similarly to some of the recent reconstruction approaches, *e.g.* Wang et al. [42], we apply the Dreambooth [35] fine-tuning approach to the SDXL model. To this end, we treat an input video \mathcal{I} as a collection of images and fine-tune the diffusion model for a given scene such that a specific text token triggers the model to follow the appearance of the scene.

3.2.1 View Sampling and Rendering Enhancement

Given the scene-personalised diffusion model, we utilise the previously trained monocular reconstruction to generate a set of pseudo-multi-view ground truth images. Firstly, we sample M sets of images for each timestep $t \in [0, T]$, effectively adding M new cameras with parameters c_m where $m \in [0, M]$ and $c_m \in \mathcal{C}_{sample}$, where \mathcal{C}_{sample} constitutes a set of new camera trajectories. To this end, we select two existing views (as a camera position and rotation), a random one, and a challenging view (with the furthest distance from the mean) and sample a new view as their weighted linear combination. To introduce variety in the difficulty of the sampled views, we gradually increase the blending weight of the views towards the most challenging ones from the input trajectory. Simultaneously, we introduce noise of an increasing amplitude to the new cameras.

Thereafter, we use our trained monocular reconstruction to render a set of M new camera views $R_{m,t}$ for each timestep. Further, we use our personalised diffusion model to enhance the rendered images

$R_{m,t} \rightarrow E_{m,t}$. This constitutes a new set of supervision images in a multi-view setting. We have chosen to generate a whole multi-view dataset in a single step instead of performing the enhancement on-the-fly. This enables the samples to be reused and reduces the computational demands (especially on GPU memory).

3.3 Diffusion-Aware Reconstruction

We use our generated dataset $\{E_{m,t}\}$ as additional supervision to re-train our 4D monocular reconstruction method to predict a higher quality output $\hat{I}_{m,t}$. However using these sampled views for training is challenging. The outputs $E_{m,t}$ of our personalised video diffusion models are high-fidelity and also preserve structure and coarse geometry, but due to the nature of the diffusion process and random noise schedule, they are not spatio-temporally consistent at the level of fine-grained detail and texture. This manifests as flickering and shifts of textures between consecutive frames. In some cases, coarse geometry may also be hallucinated, e.g. in novel viewpoints not seen during training. If we naively used these outputs to supervise monocular 4D reconstruction, the lack of spatio-temporal consistency in the training data would cause the model to either converge to a mean radiance value and cause blurry renderings, or to overfit to individual frames and learn a temporally inconsistent reconstruction. We propose the following mechanisms to overcome these challenges.

3.3.1 Dynamic Reconstruction

While dynamic regions of a scene are under-observed, static regions may be captured from multiple viewpoints across time, effectively creating multi-view supervision. Hence supervision is unnecessary in static regions and in fact could cause the quality to reduce, particularly if spatially inconsistent. We compute a mask of the dynamic regions of the scene $D_{m,t}$ using Track Anything [53], and apply this mask to our data to mask out the static regions $E_{m,t}^{dyn} = E_{m,t} \odot D_{m,t}$, where \odot denotes element-wise multiplication, and also to our predicted output $\hat{I}_{m,t}^{dyn} = \hat{I}_{m,t} \odot D_{m,t}$. This ensures that only the dynamic regions of the scene are supervised by our generated data, which reduces the convergence to the mean effect in the static reconstruction and reduces floaters. For dynamic regions, we introduce a perceptual loss [60] to encourage our reconstruction to be texturally rich and reduce blur caused by training on spatially misaligned psuedo-GTs. During training we compute the loss as $\mathcal{L}_{dyn} = |E_{m,t}^{dyn} - \hat{I}_{m,t}^{dyn}|_1 + \lambda_p |E_{m,t}^{dyn} - \hat{I}_{m,t}^{dyn}|_{vgg} + \lambda_s |E_{m,t}^{dyn} - \hat{I}_{m,t}^{dyn}|_{ssim}$, where $|\cdot|_1$ is the L1 loss, $|\cdot|_{vgg}$ is the perceptual loss using a pretrained VGG network [39], $|\cdot|_{ssim}$ is the SSIM [45] loss and λ_p and λ_s are hyperparameters set to 0.1. The dynamic loss, \mathcal{L}_{dyn} , is applied in addition to the default losses from the monocular reconstruction method, and is backpropagated to update \mathcal{G} and \mathcal{C}_{inp} .

3.3.2 Sampled Camera Pose Optimisation

Camera poses of casually captured monocular videos are typically noisy due to the difficulty of disentangling scene motion from camera motion, thus the need to optimise \mathcal{C}_{inp} in many monocular reconstruction methods [11; 44]. Our sampled camera poses \mathcal{C}_{sample} are interpolated from \mathcal{C}_{inp} and so are also noisy. As our psuedo-GTs corresponding to \mathcal{C}_{sample} are not always spatially consistent, it is even more difficult to disentangle scene motion from camera motion. To compensate for this, it is necessary to optimise our sampled camera poses during training to ensure the psuedo-GTs are aligned with the underlying scene geometry. However unlike dynamic reconstruction (Sec. 3.3.1) where we only use the dynamic masked region for supervision, we use the entire image $E_{t,m}$ as supervision for sampled camera pose optimisation. Despite fine-grained textural flickering, the coarse structure present in static regions provides a more consistent supervision signal for localisation than using only dynamic regions. We compute the loss as $\mathcal{L}_{cam} = |E_{m,t} - \hat{I}_{m,t}|_1 + \lambda_p |E_{m,t} - \hat{I}_{m,t}|_{vgg} + \lambda_s |E_{m,t} - \hat{I}_{m,t}|_{ssim}$. The camera loss, \mathcal{L}_{cam} , is backpropagated separately to other losses and only updates \mathcal{C}_{sample} .

4 Results

4.1 Datasets

We evaluate the performance of ViDAR on the DyCheck dataset [4]. DyCheck was introduced as a real world benchmark for evaluating monocular to 4D methods and is extremely challenging: the

Table 1: Quantitative results on co-visibility masked regions of scenes from the DyCheck (iPhone) dataset. Best, second and third results are highlighted in red, orange and yellow respectively. SoM-5 is full-res with wheel and space-out excluded.

	Method	PSNR-m \uparrow	SSIM-m \uparrow	LPIPS-m \downarrow
Half-Res	T-NeRF [4]	16.96	0.5772	0.3789
	NSFF [14]	15.46	0.5510	0.3960
	Nerfies [29]	16.45	0.5699	0.3389
	HyperNeRF [30]	16.81	0.5693	0.3319
	4DGS [47]	13.64	-	0.4280
	PGDVS [61]	15.88	0.5480	0.3400
	DynPoint [62]	16.89	0.5730	-
	DyBluRF [1]	17.37	0.5910	0.3730
	D-NPC [7]	16.41	0.5820	0.3190
	RoDynRF [24]	17.10	0.5340	0.5170
	Gaussian Marbles [40]	16.02	0.5416	0.3398
	SoM [44]	18.62	0.6820	0.2382
	MoSca [11]	19.32	0.7060	0.2640
Ours	19.69	0.7126	0.2231	
Full-Res	Gaussian Marbles [40]	15.84	0.5434	0.5681
	SoM [44]	17.98	0.6422	0.3718
	MoSca [11]	18.44	0.6560	0.4193
	Ours	19.00	0.6672	0.3623
SoM-5	T-NeRF [4]	15.60	0.5500	0.5500
	HyperNeRF [30]	15.99	0.5900	0.5100
	DynIBaR [15]	13.41	0.4800	0.5500
	Gaussian Marbles [40]	16.03	0.5425	0.5807
	SoM [44]	16.72	0.6300	0.4500
	CAT4D [48]	17.39	0.6070	0.3410
	MoSca [11]	18.34	0.6636	0.4321
Ours	18.76	0.6751	0.3774	

test views are far away from training views, camera poses are often inaccurate, depths are noisy and training views have issues such as overexposure and autofocus. The dataset consists of 14 casually captured scenes, 7 of which have no ground truth test views and are used for qualitative evaluation only and 7 with test views available. Due to the difficulty of obtaining accurate camera poses for all scenes, some methods choose to quantitatively evaluate on only 5 of the available 7 scenes and discard ‘space-out’ and ‘wheel’. To our knowledge, this is currently the only widely used benchmark which is appropriate for evaluating our method. As described in DyCheck [4], other datasets such as Nerfies [29], HyperNeRF [30] and NSFF [14] suffer from teleporting cameras which makes them effectively multi-view. As described in MoSca [11], the NVIDIA dataset [57] is forward-facing with small-baseline static cameras and is significantly easier than DyCheck, thus our contributions which tackle highly ill-posed settings are less useful. We quantitatively and qualitatively evaluate our method and other state of the art baselines across all 14 scenes.

4.2 Metrics

Following previous works [4; 11], we compute PSNR, SSIM and LPIPS on the co-visibility masked regions of the test views, which we denote with an $-m$ addendum to each metric. We compute metrics at both half-resolution and full-resolution, and following [44], we also report results on a subset of 5 scenes which we label SoM-5.

4.2.1 Limitations of Metrics and A New Benchmark

We note that the static regions of a scene are often observed from several viewpoints across different time steps in the captured monocular video. This effectively provides multi-view supervision for these regions, and although we are interested in reconstructing the entire scene which includes the static

Table 2: Quantitative results on dynamic regions of scenes from the DyCheck (iPhone) dataset. Best, second and third results are highlighted in red, orange and yellow respectively. SoM-5 is full-res with wheel and space-out excluded.

	Method	PSNR-D \uparrow	SSIM-D \uparrow	LPIPS-D \downarrow
Half-Res	T-NeRF [4]	13.86	0.8546	0.3491
	Nerfies [29]	12.89	0.8425	0.3811
	HyperNeRF [30]	13.27	0.8484	0.3558
	Gaussian Marbles [40]	9.99	0.8175	0.3926
	SoM [44]	14.80	0.8582	0.3008
	MoSca [11]	15.63	0.8755	0.2904
	Ours	16.46	0.8850	0.2793
Full-Res	Gaussian Marbles [40]	12.75	0.8607	0.5058
	SoM [44]	14.82	0.8709	0.4347
	MoSca [11]	15.39	0.8821	0.4413
	Ours	16.32	0.8893	0.3921
SoM-5	Gaussian Marbles [40]	13.66	0.8658	0.4919
	SoM [44]	12.50	0.8648	0.4890
	MoSca [11]	15.83	0.8872	0.4404
	Ours	16.69	0.8941	0.3778

Table 3: Intersection of co-visibility mask with dynamic regions with respect to co-visibility mask area

Scene	Dyn/Co-vis Intersection (%)
apple	4.42
block	27.46
paper-windmill	3.58
space-out	20.63
spin	19.76
teddy	81.33
wheel	24.65
mean	25.97

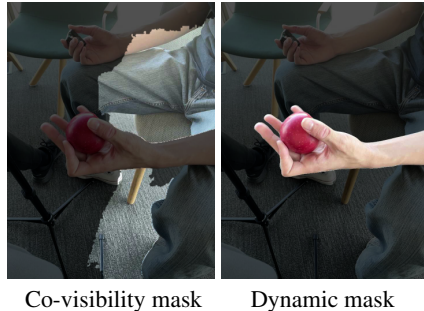


Figure 3: An example of co-visibility and dynamic mask comparison.

regions, the dynamic regions are arguably the area of most interest and also the most under-observed. In order to better evaluate performance in the dynamic regions of the scene, we compute a set of dynamic masks for each scene using Track Anything [53]. We compute the intersection between the co-visibility masks and the dynamic regions of the scene and present results in Table 3. We find that on average only 26% of the co-visibility masked pixels correspond to the dynamic region. Some scenes such as apple and paper-windmill have an intersection as low as 4%. We show an example of this in Figure 3. The co-visibility masked metrics are heavily weighted towards the static regions of the scene. Although this is useful for evaluating overall reconstruction performance, it underweights the reconstruction performance of methods in the most difficult dynamic regions. We provide a complementary new benchmark for the evaluation of monocular to 4D reconstruction methods, where our computed dynamic masks can be used in place of the commonly used co-visibility masks. We use these masks to compute the PSNR, SSIM and LPIPS, which we denote with a $-D$ addendum, for a range of baseline methods in Table 2.

4.3 Evaluation

Baselines We compare against a wide range of baselines, including a number of recent state-of-the-art methods such as MoSca [11], CAT4D [48], Shape Of Motion [44], Dynamic Gaussian Marbles [40] and 4DGS [47], which are based upon Gaussian Splatting [9]. We also compare against NeRF-based approaches T-NeRF [4], Nerfies [29], HyperNeRF [30], DyBluRF [1] and RoDynRF [24],

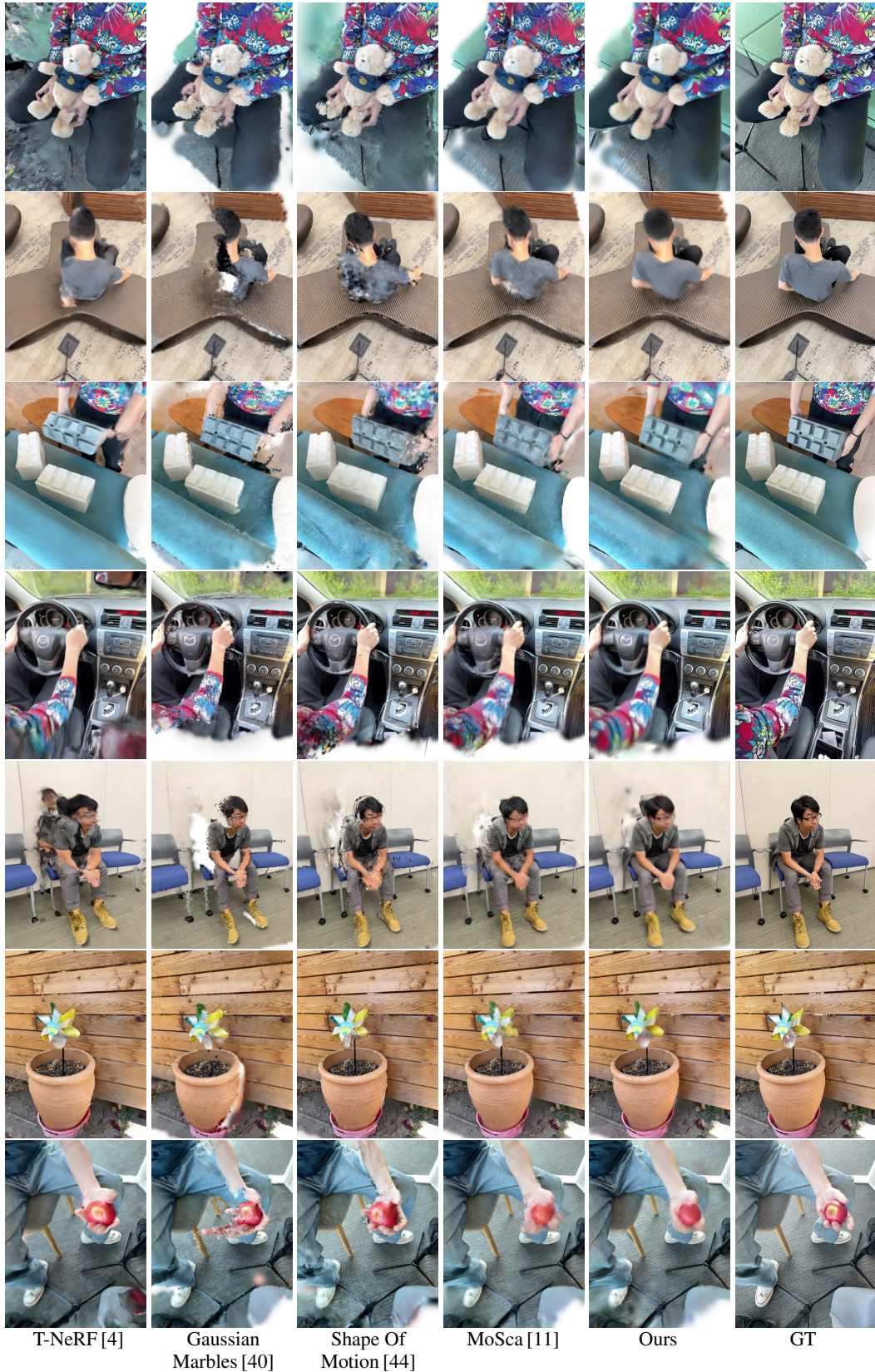


Figure 4: Qualitative evaluation of our method against benchmark methods on the DyCheck test set.

Table 4: Quantitative results of an ablation study of the components of ViDAR.

Method	PSNR-m	SSIM-m	LPIPS-m
Ours	19.00	0.6672	0.3623
W/o Tracking Based Gaussian Classification (TGS)	18.88	0.6651	0.3693
W/o Sampled Camera Optimisation (SO)	18.39	0.6514	0.4040
W/o Dynamic Reconstruction (DR)	18.93	0.6274	0.4497
W/o SO + DR + TGS	18.46	0.6075	0.4656

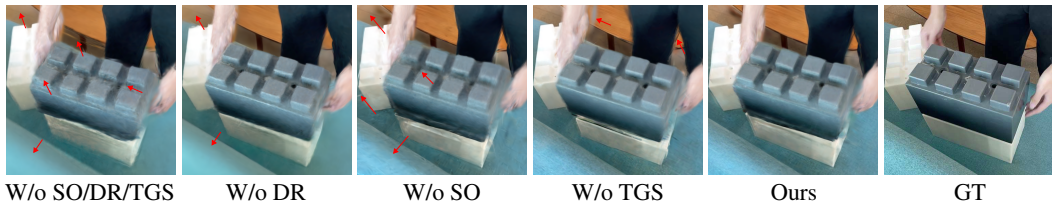


Figure 5: Qualitative evaluation of our ablation study with settings corresponding to Tab. 4.

neural point clouds approaches DynPoint [62] and D-NPC [7], generalized pre-trained transformer PGDVS [61], neural scene flow NSFF [14] and volumetric image-based rendering DynIBaR [15].

Quantitative and Qualitative Evaluation We present quantitative results of our method in Tables 1 and 2. Our method outperforms all state-of-the-art baselines in PSNR and SSIM and all but one in LPIPS, across all settings and resolutions. We typically improve PSNR by a large margin, achieving a minimum of 1dB improvement over all methods, except for MoSca where we average 0.94dB and 0.56dB higher in dynamic and co-visibility masked regions respectively. This indicates our method particularly improves dynamic region reconstruction. We note that CAT4D achieves a lower LPIPS score than our method, but the improved perceptual quality comes at the cost of reduced spatio-temporal consistency, which is reflected in the PSNR and SSIM scores, and also clearly shown in our supplementary video. We present a qualitative evaluation in Figure 4 where ViDAR demonstrates consistently superior visual quality and geometric consistency when compared to the best existing approaches. Although 2D image comparisons are indicative of performance, we encourage viewing our supplementary video results to appreciate the improvement in spatio-temporal consistency and visual quality over baselines.

Ablations We quantitatively evaluate each of our contributions in an ablation study presented in Table 4. The bottom row w/o SO + DR + TGS shows a naive approach of using the diffused novel views directly as supervision for our monocular baseline without diffusion-aware reconstruction. Due to the spatio-temporal inconsistencies of the diffused outputs, this leads to a poor quality reconstruction, as shown in Figure 5. We show that removing dynamic reconstruction leads to blurry reconstruction in static regions, while removing sampled camera optimization leads to geometric inconsistencies. We also show that using our tracking based Gaussian classification reduces floaters.

5 Conclusion

We present ViDAR, a novel method for 4D reconstruction of scenes from monocular inputs. ViDAR leverages video diffusion models by conditioning on scene-specific features to recover fine-grained appearance details of novel viewpoints. ViDAR overcomes the spatio-temporal inconsistency of diffusion-based supervision via a diffusion-aware loss function and a camera pose optimisation strategy. We show that ViDAR outperforms all state-of-the-art baselines on the challenging DyCheck dataset, and we present a new benchmark to evaluate performance in dynamic regions.

Limitations: ViDAR limits the scope of diffusion to enhancing rendered images, which are limited by the initial accuracy of the 4D reconstruction, thus, cannot repair major geometrical artefacts.

References

- [1] M.-Q. V. Bui, J. Park, J. Oh, and M. Kim. DyBluRF: Dynamic Deblurring Neural Radiance Fields for Blurry Monocular Video. *arXiv preprint arXiv:2312.13528*, 2023.
- [2] A. Cao and J. CV. HexPlane: A Fast Representation for Dynamic Scenes. In *Computer Vision and Pattern Recognition Conference (CVPR)*, 2023.
- [3] S. Fridovich-Keil, G. Meanti, F. R. Warburg, B. Recht, and A. Kanazawa. K-Planes: Explicit Radiance Fields in Space, Time, and Appearance. In *Computer Vision and Pattern Recognition Conference (CVPR)*, 2023.
- [4] H. Gao, R. Li, S. Tulsiani, B. Russell, and A. Kanazawa. Monocular Dynamic View Synthesis: A Reality Check. In *Conference on Neural Information Processing Systems*, 2022.
- [5] V. Guizilini, M. Z. Irshad, D. Chen, G. Shakhnarovich, and R. Ambrus. Zero-Shot Novel View and Depth Synthesis with Multi-View Geometric Diffusion. In *Computer Vision and Pattern Recognition Conference (CVPR)*, 2025.
- [6] Y.-H. Huang, Y.-T. Sun, Z. Yang, X. Lyu, Y.-P. Cao, and X. Qi. SC-GS: Sparse-Controlled Gaussian Splatting for Editable Dynamic Scenes. In *Computer Vision and Pattern Recognition Conference (CVPR)*, 2023.
- [7] M. Kappel, F. Hahlbohm, T. Scholz, S. Castillo, C. Theobalt, M. Eisemann, V. Golyanik, and M. Magnor. D-NPC: Dynamic neural point clouds for non-rigid view synthesis from monocular video. *Proceedings of the Eurographics Conference (EG)*, 44, 2025.
- [8] T. Karras, M. Aittala, T. Aila, and S. Laine. Elucidating the design space of diffusion-based generative models. In *Conference on Neural Information Processing Systems*, 2022.
- [9] B. Kerbl, G. Kopanas, T. Leimkühler, and G. Drettakis. 3D Gaussian Splatting for Real-Time Radiance Field Rendering. *ACM Transactions on Graphics*, 42(4), July 2023.
- [10] J. Lee, C. Won, H. Jung, I. Bae, and H.-G. Jeon. Fully Explicit Dynamic Gaussian Splatting. In *Proceedings of the Neural Information Processing Systems*, 2024.
- [11] J. Lei, Y. Weng, A. Harley, L. Guibas, and K. Daniilidis. MoSca: Dynamic gaussian fusion from casual videos via 4D motion scaffolds. *Computer Vision and Pattern Recognition Conference (CVPR)*, 2025.
- [12] H. Li, H. Shi, W. Zhang, W. Wu, Y. Liao, L. Wang, L.-h. Lee, and P. Y. Zhou. Dreamscene: 3d gaussian-based text-to-3d scene generation via formation pattern sampling. In *European Conference on Computer Vision (ECCV)*, 2024.
- [13] L. Li, Z. Shen, Z. Wang, L. Shen, and P. Tan. Streaming Radiance Fields for 3D Video Synthesis. In *Conference on Neural Information Processing Systems*, 2022.
- [14] Z. Li, S. Niklaus, N. Snavely, and O. Wang. Neural Scene Flow Fields for Space-Time View Synthesis of Dynamic Scenes. In *Computer Vision and Pattern Recognition Conference (CVPR)*, 2021.
- [15] Z. Li, Q. Wang, F. Cole, R. Tucker, and N. Snavely. DynIBaR: Neural Dynamic Image-Based Rendering. In *Computer Vision and Pattern Recognition Conference (CVPR)*, 2023.
- [16] Z. Li, Z. Chen, Z. Li, and Y. Xu. Spacetime Gaussian Feature Splatting for Real-Time Dynamic View Synthesis. In *Computer Vision and Pattern Recognition Conference (CVPR)*, 2024.
- [17] H. Liang, J. Ren, A. Mirzaei, A. Torralba, Z. Liu, I. Gilitschenski, S. Fidler, C. Oztireli, H. Ling, Z. Gojcic, and J. Huang. Feed-Forward Bullet-Time Reconstruction of Dynamic Scenes from Monocular Videos. *arXiv preprint arXiv:2412.03526*, 2024.
- [18] Y. Liang, X. Yang, J. Lin, H. Li, X. Xu, and Y. Chen. Luciddreamer: Towards high-fidelity text-to-3d generation via interval score matching. In *Computer Vision and Pattern Recognition Conference (CVPR)*, 2024.
- [19] C. Lin, P. Pan, B. Yang, Z. Li, and Y. Mu. DiffSplat: Repurposing Image Diffusion Models for Scalable 3D Gaussian Splat Generation. In *International Conference on Learning Representations (ICLR)*, 2025.
- [20] Y. Lin, Z. Dai, S. Zhu, and Y. Yao. Gaussian-Flow: 4D Reconstruction with Dynamic 3D Gaussian Particle. In *Computer Vision and Pattern Recognition Conference (CVPR)*, 2024.

- [21] M. Liu, R. Shi, L. Chen, Z. Zhang, C. Xu, X. Wei, H. Chen, C. Zeng, J. Gu, and H. Su. One-2-3-45++: Fast Single Image to 3D Objects with Consistent Multi-View Generation and 3D Diffusion. In *Computer Vision and Pattern Recognition Conference (CVPR)*, 2024.
- [22] M. Liu, C. Zeng, X. Wei, R. Shi, L. Chen, C. Xu, M. Zhang, Z. Wang, X. Zhang, I. Liu, H. Wu, and H. Su. MeshFormer: High-Quality Mesh Generation with 3D-Guided Reconstruction Model. In *Conference on Neural Information Processing Systems*, 2024.
- [23] Q. Liu, Y. Liu, J. Wang, X. Lyu, P. Wang, W. Wang, and J. Hou. MoDGS: Dynamic Gaussian Splatting from Casually-captured Monocular Videos with Depth Priors. In *International Conference on Learning Representations (ICLR)*, 2025.
- [24] Y.-L. Liu, C. Gao, A. Meuleman, H.-Y. Tseng, A. Saraf, C. Kim, Y.-Y. Chuang, J. Kopf, and J.-B. Huang. Robust dynamic radiance fields. In *Computer Vision and Pattern Recognition Conference (CVPR)*, 2023.
- [25] J. Luiten, G. Kopanas, B. Leibe, and D. Ramanan. Dynamic 3D Gaussians: Tracking by Persistent Dynamic View Synthesis. In *International Conference on 3D Vision (3DV)*, 2024.
- [26] X. Miao, Y. Bai, H. Duan, F. Wan, Y. Huang, Y. Long, and Y. Zheng. CTNeRF: Cross-time Transformer for dynamic neural radiance field from monocular video. *Pattern Recognition*, 156:110729, 2024.
- [27] B. Mildenhall, P. P. Srinivasan, M. Tancik, J. T. Barron, R. Ramamoorthi, and R. Ng. NeRF: Representing scenes as neural radiance fields for view synthesis. In *European Conference on Computer Vision (ECCV)*, 2020.
- [28] J. Park, M.-Q. V. Bui, J. L. G. Bello, J. Moon, J. Oh, and M. Kim. SplineGS: Robust Motion-Adaptive Spline for Real-Time Dynamic 3D Gaussians from Monocular Video. In *Computer Vision and Pattern Recognition Conference (CVPR)*, 2025.
- [29] K. Park, U. Sinha, J. T. Barron, S. Bouaziz, D. B. Goldman, S. M. Seitz, and R. Martin-Brualla. Nerfies: Deformable Neural Radiance Fields. *International Conference on Computer Vision (ICCV)*, 2021.
- [30] K. Park, U. Sinha, P. Hedman, J. T. Barron, S. Bouaziz, D. B. Goldman, R. Martin-Brualla, and S. M. Seitz. HyperNeRF: a higher-dimensional representation for topologically varying neural radiance fields. *ACM Transactions on Graphics*, 40(6), 2021.
- [31] D. Podell, Z. English, K. Lacey, A. Blattmann, T. Dockhorn, J. Müller, J. Penna, and R. Rombach. SDXL: Improving Latent Diffusion Models for High-Resolution Image Synthesis. In *International Conference on Learning Representations (ICLR)*, 2024.
- [32] B. Poole, A. Jain, J. T. Barron, and B. Mildenhall. DreamFusion: Text-to-3D using 2D Diffusion. In *International Conference on Learning Representations (ICLR)*, 2023.
- [33] A. Pumarola, E. Corona, G. Pons-Moll, and F. Moreno-Noguer. D-NeRF: Neural Radiance Fields for Dynamic Scenes. In *Computer Vision and Pattern Recognition Conference (CVPR)*, 2021.
- [34] R. Rombach, A. Blattmann, D. Lorenz, P. Esser, and B. Ommer. High-resolution image synthesis with latent diffusion models. In *Computer Vision and Pattern Recognition Conference (CVPR)*, 2021.
- [35] N. Ruiz, Y. Li, V. Jampani, Y. Pritch, M. Rubinstein, and K. Aberman. DreamBooth: Fine Tuning Text-to-image Diffusion Models for Subject-Driven Generation. In *Computer Vision and Pattern Recognition Conference (CVPR)*, 2023.
- [36] R. Shao, Z. Zheng, H. Tu, B. Liu, H. Zhang, and Y. Liu. Tensor4D: Efficient Neural 4D Decomposition for High-fidelity Dynamic Reconstruction and Rendering. In *Computer Vision and Pattern Recognition Conference (CVPR)*, 2023.
- [37] R. Shaw, M. Nazarczuk, J. Song, A. Moreau, S. Catley-Chandar, H. Dharmo, and E. Pérez-Pellitero. SWinGS: Sliding Windows for Dynamic 3D Gaussian Splatting. In *European Conference on Computer Vision (ECCV)*, 2024.
- [38] J. Shriram, A. Trevithick, L. Liu, and R. Ramamoorthi. RealmDreamer: Text-Driven 3D Scene Generation with Inpainting and Depth Diffusion. In *International Conference on 3D Vision (3DV)*, 2025.
- [39] K. Simonyan and A. Zisserman. Very deep convolutional networks for large-scale image recognition. In *International Conference on Learning Representations*, 2015.
- [40] C. Stearns, A. W. Harley, M. Uy, F. Dubost, F. Tombari, G. Wetzstein, and L. Guibas. Dynamic Gaussian Marbles for Novel View Synthesis of Casual Monocular Videos. In *SIGGRAPH Asia*, 2024.

- [41] J. Tang, Z. Chen, X. Chen, T. Wang, G. Zeng, and Z. Liu. LGM: Large Multi-View Gaussian Model for High-Resolution 3D Content Creation. In *European Conference on Computer Vision (ECCV)*, 2024.
- [42] C. Wang, P. Zhuang, A. Siarohin, J. Cao, G. Qian, H.-Y. Lee, and S. Tulyakov. Diffusion Priors for Dynamic View Synthesis from Monocular Videos. *arXiv preprint arXiv:2401.05583*, 2024.
- [43] F. Wang, S. Tan, X. Li, Z. Tian, and H. Liu. Mixed Neural Voxels for Fast Multi-view Video Synthesis. In *International Conference on Computer Vision (ICCV)*, 2023.
- [44] Q. Wang, V. Ye, H. Gao, W. Zeng, J. Austin, Z. Li, and A. Kanazawa. Shape of Motion: 4D Reconstruction from a Single Video. In *arXiv preprint arXiv:2407.13764*, 2024.
- [45] Z. Wang, A. Bovik, H. Sheikh, and E. Simoncelli. Image quality assessment: from error visibility to structural similarity. *IEEE TIP*, 13(4), 2004.
- [46] T. Wimmer, M. Oechsle, M. Niemeyer, and F. Tombari. Gaussians-to-Life: Text-Driven Animation of 3D Gaussian Splatting Scenes. In *International Conference on 3D Vision (3DV)*, 2025.
- [47] G. Wu, T. Yi, J. Fang, L. Xie, X. Zhang, W. Wei, W. Liu, Q. Tian, and X. Wang. 4D Gaussian Splatting for Real-Time Dynamic Scene Rendering. In *Computer Vision and Pattern Recognition Conference (CVPR)*, 2024.
- [48] R. Wu, R. Gao, B. Poole, A. Trevisan, C. Zheng, J. T. Barron, and A. Holynski. CAT4D: Create Anything in 4D with Multi-View Video Diffusion Models. *arXiv:2411.18613*, 2024.
- [49] R. Wu, B. Mildenhall, P. Henzler, K. Park, R. Gao, D. Watson, P. P. Srinivasan, D. Verbin, J. T. Barron, B. Poole, and A. Holynski. ReconFusion: 3D Reconstruction with Diffusion Priors. In *Computer Vision and Pattern Recognition Conference (CVPR)*, 2024.
- [50] J. Xu, W. Cheng, Y. Gao, X. Wang, S. Gao, and Y. Shan. Instantmesh: Efficient 3d mesh generation from a single image with sparse-view large reconstruction models. *arXiv preprint arXiv:2404.07191*, 2024.
- [51] Y. Xu, H. Tan, F. Luan, S. Bi, P. Wang, J. Li, Z. Shi, K. Sunkavalli, G. Wetzstein, Z. Xu, and K. Zhang. DMV3D: Denoising Multi-View Diffusion using 3D Large Reconstruction Model. In *International Conference on Learning Representations (ICLR)*, 2024.
- [52] C. Yang, S. Li, J. Fang, R. Liang, L. Xie, X. Zhang, W. Shen, and Q. Tian. GaussianObject: High-Quality 3D Object Reconstruction from Four Views with Gaussian Splatting. In *SIGGRAPH Asia*, 2024.
- [53] J. Yang, M. Gao, Z. Li, S. Gao, F. Wang, and F. Zheng. Track Anything: Segment Anything Meets Videos. *arXiv preprint arXiv:2304.11968*, 2023.
- [54] S. Yang, W. Yu, J. Zeng, J. Lv, K. Ren, C. Lu, D. Lin, and J. Pang. Novel demonstration generation with gaussian splatting enables robust one-shot manipulation. *arXiv preprint arXiv:2504.13175*, 2025.
- [55] Z. Yang, X. Gao, W. Zhou, S. Jiao, Y. Zhang, and X. Jin. Deformable 3D Gaussians for High-Fidelity Monocular Dynamic Scene Reconstruction. In *Computer Vision and Pattern Recognition Conference (CVPR)*, 2024.
- [56] T. Yi, J. Fang, J. Wang, G. Wu, L. Xie, X. Zhang, W. Liu, Q. Tian, and X. Wang. GaussianDreamer: Fast Generation from Text to 3D Gaussians by Bridging 2D and 3D Diffusion Models. In *Computer Vision and Pattern Recognition Conference (CVPR)*, 2024.
- [57] J. S. Yoon, K. Kim, O. Gallo, H. S. Park, and J. Kautz. Novel view synthesis of dynamic scenes with globally coherent depths from a monocular camera. In *Computer Vision and Pattern Recognition Conference (CVPR)*, 2020.
- [58] H. Yu, C. Wang, P. Zhuang, W. Menapace, A. Siarohin, J. Cao, L. A. Jeni, S. Tulyakov, and H.-Y. Lee. 4Real: Towards Photorealistic 4D Scene Generation via Video Diffusion Models. In *Conference on Neural Information Processing Systems*, 2024.
- [59] Y. Zeng, Y. Jiang, S. Zhu, Y. Lu, Y. Lin, H. Zhu, W. Hu, X. Cao, and Y. Yao. STAG4D: Spatial-Temporal Anchored Generative 4D Gaussians. In *European Conference on Computer Vision (ECCV)*, 2024.
- [60] R. Zhang, P. Isola, A. A. Efros, E. Shechtman, and O. Wang. The Unreasonable Effectiveness of Deep Features as a Perceptual Metric. In *Computer Vision and Pattern Recognition Conference (CVPR)*, 2018.
- [61] X. Zhao, A. Colburn, F. Ma, M. Ángel Bautista, J. M. Susskind, and A. G. Schwing. Pseudo-Generalized Dynamic View Synthesis from a Video. In *International Conference on Learning Representations (ICLR)*, 2024.

- [62] K. Zhou, J.-X. Zhong, S. Shin, K. Lu, Y. Yang, A. Markham, and N. Trigoni. DynPoint: dynamic neural point for view synthesis. In *Conference on Neural Information Processing Systems*, 2023.
- [63] R. Zhu, Y. Liang, H. Chang, J. Deng, J. Lu, W. Yang, T. Zhang, and Y. Zhang. MotionGS: Exploring Explicit Motion Guidance for Deformable 3D Gaussian Splatting. In *Conference on Neural Information Processing Systems*, 2024.
- [64] Z.-X. Zou, Z. Yu, Y.-C. Guo, Y. Li, D. Liang, Y.-P. Cao, and S.-H. Zhang. Triplane Meets Gaussian Splatting: Fast and Generalizable Single-View 3D Reconstruction with Transformers. In *Computer Vision and Pattern Recognition Conference (CVPR)*, 2024.

ViDAR: Video Diffusion-Aware 4D Reconstruction From Monocular Inputs

Supplementary Material

A Additional Results

In this section, we include additional qualitative and quantitative evaluation of ViDAR.

A.1 Further Qualitative Evaluation

We present additional qualitative evaluation of ViDAR compared to MoSca and Shape Of Motion on the qualitative example scenes from the DyCheck dataset in Fig. 6. Our results show consistently greater geometric consistency and visual quality compared to the other approaches.

A.2 Per-Scene Results

We provide a detailed quantitative evaluation for every scene of the DyCheck dataset in Tables 5 and 6, in half and full resolution respectively. As in Tables 1 and 2, we compute PSNR, SSIM and LPIPS on the co-visibility masked regions of the test views, which we denote with an $-m$ addendum to each metric, as well as on the dynamic masked regions of the test views which we denote with a $-D$. With a few exceptions (e.g. Apple, co-visibility), ViDAR is consistently the best performing method.

B Implementation Details

In this section, we provide any implementation details not included in the main manuscript.

B.1 Monocular Reconstruction

We implement the monocular reconstruction step directly as MoSca [11], keeping the original hyperparameters intact. We substitute dynamic masks estimated from epipolar error by masks obtained from Track Anything [53].

B.2 Personalised Diffusion Model

We train our personalised diffusion model with a Dreambooth [35] approach implemented in the `diffusers`² library as a LoRA fine-tuning process. We use the default implementation of the SDXL model with default parameters. We change the resolution to match our input resolution (720x960). Similarly, we change the number of training iterations from the default 500 to 5000, in response to the default model being suitable for personalisation with a smaller number of images (5-40), as opposed to our inputs (ranging above 400).

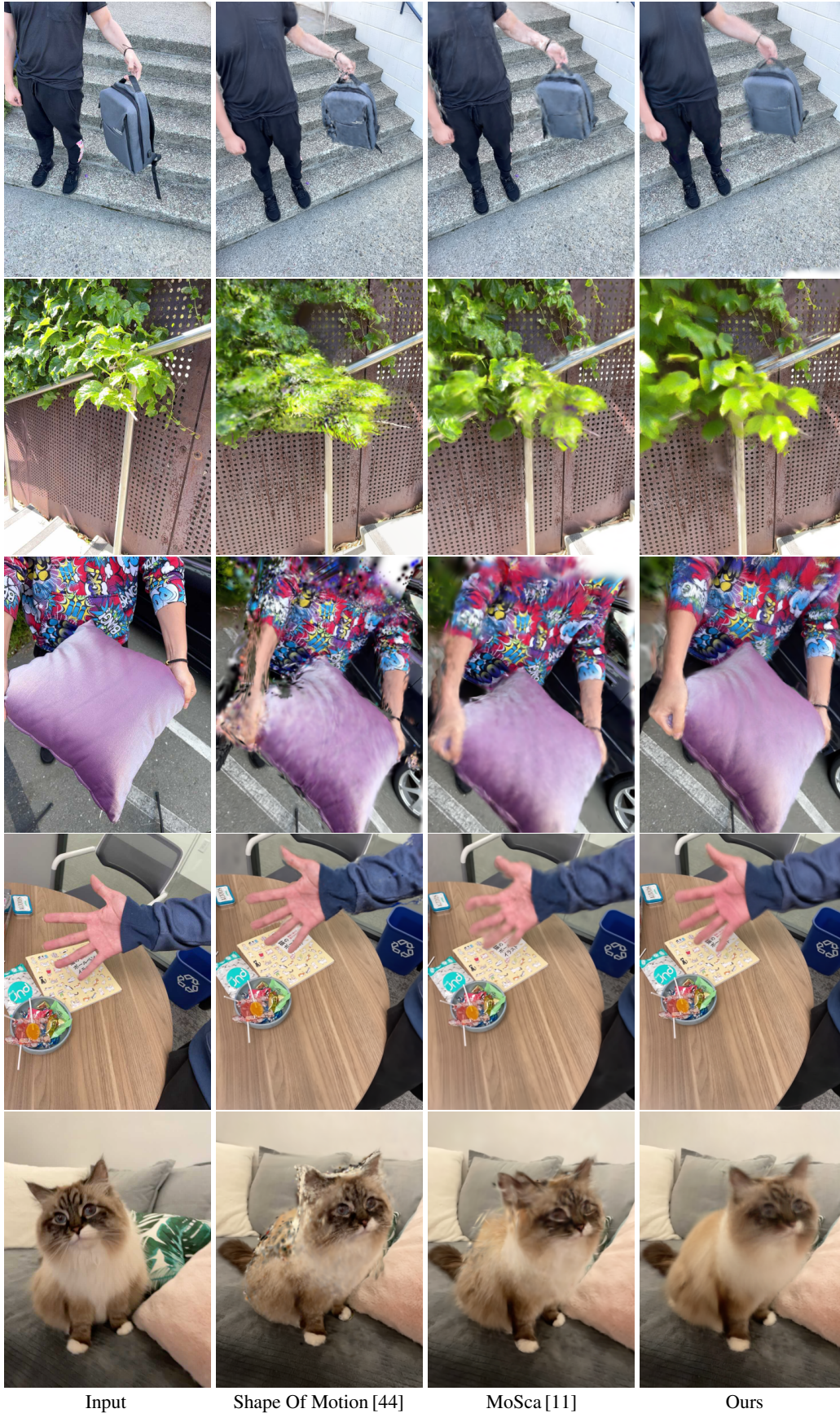
B.3 Camera Sampling

To obtain a set of varying samples for multi-view supervision, we propose a camera sampling strategy based on extreme poses within the input trajectory.

²<https://huggingface.co/docs/diffusers>

Table 5: Per-scene quantitative evaluation of ViDAR against state-of-the-art methods on the DyCheck dataset at half resolution. Best, second and third results are highlighted in red, orange and yellow respectively.

	Method	PSNR-m \uparrow	SSIM-m \uparrow	LPIPS-m \downarrow	PSNR-D \uparrow	SSIM-D \uparrow	LPIPS-D \downarrow
Apple	T-NeRF [4]	17.43	0.7285	0.5081	13.63	0.9433	0.3108
	Nerfies [29]	17.54	0.7505	0.4785	13.63	0.9437	0.3321
	HyperNeRF [30]	17.64	0.7433	0.4775	13.36	0.9417	0.3362
	Gaussian Marbles [40]	17.90	0.7328	0.4716	14.56	0.9370	0.3229
	SoM [44]	18.95	0.8111	0.2917	14.88	0.9419	0.3016
	MoSca [11]	19.40	0.8074	0.3392	16.97	0.9580	0.2176
	Ours	19.18	0.8008	0.3149	17.75	0.9616	0.1893
Block	T-NeRF [4]	17.52	0.6688	0.3460	14.07	0.8591	0.3474
	Nerfies [29]	16.61	0.6393	0.3893	13.31	0.8433	0.4068
	HyperNeRF [30]	17.54	0.6702	0.3312	13.73	0.8525	0.3483
	Gaussian Marbles [40]	16.95	0.6509	0.3788	13.81	0.8480	0.3750
	SoM [44]	17.99	0.6634	0.2608	15.23	0.8596	0.3378
	MoSca [11]	18.11	0.6801	0.3416	15.32	0.8699	0.3499
	Ours	18.91	0.6901	0.2168	15.93	0.8864	0.3052
Paper	T-NeRF [4]	17.55	0.3672	0.2577	12.50	0.9730	0.3149
	Nerfies [29]	17.34	0.3783	0.2111	10.84	0.9710	0.3929
	HyperNeRF [30]	17.38	0.3819	0.2086	10.64	0.9706	0.4040
	Gaussian Marbles [40]	16.62	0.3219	0.3517	11.68	0.9710	0.2680
	SoM [44]	20.85	0.6725	0.1536	12.90	0.9738	0.2634
	MoSca [11]	22.24	0.7450	0.1617	14.32	0.9789	0.2832
	Ours	22.48	0.7516	0.1287	15.58	0.9807	0.3080
Space-out	T-NeRF [4]	17.71	0.5914	0.3768	14.52	0.8620	0.3649
	Nerfies [29]	17.79	0.6217	0.3032	13.85	0.8578	0.3407
	HyperNeRF [30]	17.93	0.6054	0.3203	14.26	0.8597	0.3379
	Gaussian Marbles [40]	15.32	0.5512	0.4235	11.15	0.8488	0.4278
	SoM [44]	19.64	0.6313	0.2374	15.72	0.8805	0.2429
	MoSca [11]	20.35	0.6582	0.2702	17.57	0.8985	0.2073
	Ours	21.58	0.6890	0.2010	18.77	0.9091	0.2306
Spin	T-NeRF [4]	19.16	0.5672	0.4427	15.65	0.9090	0.3394
	Nerfies [29]	18.38	0.5846	0.3087	14.11	0.8899	0.3868
	HyperNeRF [30]	19.20	0.5614	0.3254	15.65	0.9060	0.3230
	Gaussian Marbles [40]	18.31	0.5461	0.3558	15.68	0.8963	0.3950
	SoM [44]	21.05	0.7798	0.1698	18.44	0.9180	0.2815
	MoSca [11]	21.06	0.7100	0.2084	18.85	0.9240	0.2688
	Ours	21.28	0.7209	0.1853	19.37	0.9327	0.2566
Teddy	T-NeRF [4]	13.71	0.5695	0.4286	13.49	0.6198	0.3730
	Nerfies [29]	13.65	0.5572	0.3716	13.33	0.6050	0.3280
	HyperNeRF [30]	13.97	0.5678	0.3498	13.65	0.6168	0.3028
	Gaussian Marbles [40]	13.65	0.5432	0.4369	13.29	0.5972	0.3961
	SoM [44]	14.00	0.5462	0.3399	13.68	0.5998	0.3335
	MoSca [11]	15.09	0.6133	0.3587	14.84	0.6679	0.3146
	Ours	15.97	0.6416	0.3096	15.62	0.6844	0.2901
Wheel	T-NeRF [4]	15.65	0.5481	0.2925	13.19	0.8162	0.3937
	Nerfies [29]	13.82	0.4580	0.3097	11.15	0.7870	0.4805
	HyperNeRF [30]	13.99	0.4550	0.3102	11.60	0.7913	0.4385
	Gaussian Marbles [40]	16.02	0.5416	0.3398	9.99	0.8175	0.3926
	SoM [44]	17.86	0.6695	0.2144	12.75	0.8338	0.3446
	MoSca [11]	17.95	0.6852	0.2309	11.57	0.8310	0.3918
	Ours	18.46	0.6943	0.2058	12.23	0.8402	0.3754



Input

Shape Of Motion [44]

MoSca [11]

Ours

Figure 6: Qualitative evaluation of our method against benchmark methods on the DyCheck qualitative example set.

Table 6: Per-scene quantitative evaluation of ViDAR against state-of-the-art methods on the DyCheck dataset at full resolution. Best, second and third results are highlighted in red, orange and yellow respectively.

	Method	PSNR-m \uparrow	SSIM-m \uparrow	LPIPS-m \downarrow	PSNR-D \uparrow	SSIM-D \uparrow	LPIPS-D \downarrow
Apple	Gaussian Marbles [40]	16.84	0.7022	0.6849	14.65	0.9495	0.4281
	SoM [44]	17.74	0.7535	0.4946	14.88	0.9540	0.4036
	MoSca [11]	18.19	0.7486	0.5651	17.21	0.9681	0.3073
	Ours	18.02	0.7466	0.5359	18.07	0.9694	0.2559
Block	Gaussian Marbles [40]	16.50	0.6492	0.5065	13.49	0.8660	0.4987
	SoM [44]	17.42	0.6566	0.3879	14.60	0.8759	0.4667
	MoSca [11]	17.56	0.6710	0.4658	14.97	0.8848	0.4808
	Ours	18.43	0.6722	0.3932	15.54	0.8898	0.4100
Paper	Gaussian Marbles [40]	15.96	0.2959	0.5778	11.30	0.9722	0.5094
	SoM [44]	19.65	0.5518	0.2035	13.03	0.9737	0.4861
	MoSca [11]	20.82	0.6289	0.2412	14.04	0.9770	0.5498
	Ours	21.06	0.6477	0.1923	14.99	0.9777	0.5003
Space-out	Gaussian Marbles [40]	15.19	0.5603	0.5434	11.07	0.8671	0.5334
	SoM [44]	19.54	0.6178	0.3667	16.11	0.8939	0.3363
	MoSca [11]	19.93	0.6280	0.4060	17.17	0.8988	0.3207
	Ours	21.15	0.6443	0.3278	18.56	0.9079	0.3356
Spin	Gaussian Marbles [40]	17.84	0.5154	0.4784	15.79	0.9143	0.4420
	SoM [44]	20.57	0.7323	0.2663	18.65	0.9339	0.3535
	MoSca [11]	20.61	0.6769	0.3108	18.50	0.9371	0.3657
	Ours	20.69	0.6851	0.2868	19.37	0.9445	0.3094
Teddy	Gaussian Marbles [40]	13.01	0.5496	0.6559	13.05	0.6269	0.5815
	SoM [44]	13.58	0.5518	0.5377	13.40	0.6251	0.4928
	MoSca [11]	14.52	0.5925	0.5777	14.41	0.6692	0.4986
	Ours	15.63	0.6238	0.4786	15.46	0.6892	0.4133
Wheel	Gaussian Marbles [40]	15.55	0.5310	0.5295	9.89	0.8291	0.5473
	SoM [44]	17.38	0.6318	0.3456	13.05	0.8393	0.5037
	MoSca [11]	17.49	0.6460	0.3684	11.42	0.8395	0.5665
	Ours	18.00	0.6505	0.3215	12.21	0.8469	0.5203

Given the set of input camera poses (position and orientation), we calculate a mean camera pose. Then, we establish a sphere approximating the surface established by the input trajectory, assuming that a target dynamic object is being tracked by the recording. Finally, we select two views in the input trajectory that, when projected on the sphere, are characterised by the largest longitudinal displacement. These constitute the extreme camera poses.

Thereafter, for each time step spanning the whole time range of the input video, we sample the following new cameras:

- Two random camera poses from the input trajectory are selected, and a new camera pose is calculated as their mean, and random noise is added. Total cameras: 4
- For each of the two extreme views, a random camera pose from the input trajectory is selected, and a new camera pose is calculated as their weighted average, and random noise is added, with the weight increasing towards the extreme views. Total cameras: 12
- The extreme camera views. Total cameras: 2

This constitutes our set of 18 new training cameras for each timestep of the input video $c_m \in \mathcal{C}_{sample}$.

B.4 Multi-View Sample Enhancement

Having sampled a set of new trajectories, we render them with the previously trained monocular reconstruction model, in such way we obtain a set of degraded images $\{R_{m,t}\}$. To perform the

enhancement as described in Section 3.2, we utilise the Image2Image translation approach as implemented in `diffusers`.

B.5 Diffusion-Aware Reconstruction

We increase the total number of iterations from 8000 to 40000 in order to train on the additional generated data. During optimisation, we run two separate forward and backward passes, the first for sampled camera pose optimisation and the second for optimising the Gaussians and input camera poses. At each iteration, we randomly select two of the sampled camera poses which correspond to the same time step as the input camera. During the first pass, we render the images and compute the mean of the camera losses \mathcal{L}_{cam} for both of the sampled cameras and update only the sampled camera poses \mathcal{C}_{sample} . During the second pass, we re-render the images using the updated camera poses and compute the dynamic loss \mathcal{L}_{dyn} using the dynamic region masks. This loss is added to the existing monocular losses and is used to update the input camera poses \mathcal{C}_{inp} and the Gaussians \mathcal{G} .